ELSEVIER

Contents lists available at ScienceDirect

International Journal of Fatigue

journal homepage: www.elsevier.com/locate/ijfatigue





Fatigue assessment of additively-manufactured C-18150 copper alloy at room and elevated temperatures via a microstructure-sensitive algorithm

Arash P. Jirandehi a, M.M. Khonsari a, S. Guo a, Paul Gradl b

- ^a Louisiana State University, Department of Mechanical and Industrial Engineering, Baton Rouge, LA 70803, USA
- b NASA Marshall Space Flight Center, ER13 Component Technology Development, Huntsville, AL 35812, USA

ARTICLE INFO

Keywords:
Additive manufacturing
Fatigue
Fracture fatigue entropy
Plastic strain energy
Microstructure

ABSTRACT

The efficacy of a recently developed microstructure-sensitive fatigue framework is assessed for additively manufactured materials at different environmental temperatures. C-18150 copper alloy samples additively manufactured using the Laser Powder Bed Fusion process (L-PBF) are fatigue tested at the room, 204 °C, and 426 °C temperatures. Plastic strain energy as the damage representative is studied via the cyclic stress–strain hysteresis loop area measurements and analyzed via a microstructure-sensitive algorithm. A thermodynamics-based framework is used to calculate Fracture Fatigue Entropy (FFE) to assess the material's fatigue performance. The results based on the hysteresis loop and the microstructure-sensitive method agree both in trend and magnitude.

1. Introduction

Emerging materials produced with advanced manufacturing processes such as additive manufacturing (AM) are expected to advance many applications across various industries with a strong focus in aerospace. In general, 70-90 percent of the structural damages/failures occur due to fatigue [1]. In particular, 55% of the failures in aircraft components are reported to be solely due to mechanical fatigue degradation [2]. The problem has become substantially more complex when dealing with AM components. Generally, AM metallic alloys contain a large number of defects—such as manufacturing pores, voids, un-melted particles, and lack-of-fusion defects—in addition to the point and planar defects compared to the conventionally produced alloys. When exposed to cyclic loading, these defects are the root cause and primary sites of fatigue damage accumulation and cracks nucleation. This has been verified by testing polished specimens prepared according to ASTM fatigue standard [3-11]. Readers interested in the effect of surface roughness (SR) on the fatigue of AM specimens with as-built surface vs. the polished/machined ones are referred to Refs. [12-14]. In all cases, considering the role of microstructure when estimating the fatigue damage in additively manufactured specimens is vitally important [3,15-17].

The existing literature contains experimental, theoretical, and numerical efforts to quantify fatigue damage/life that consider the role of defects [1,3,18]. Noteworthy contributions were reported by

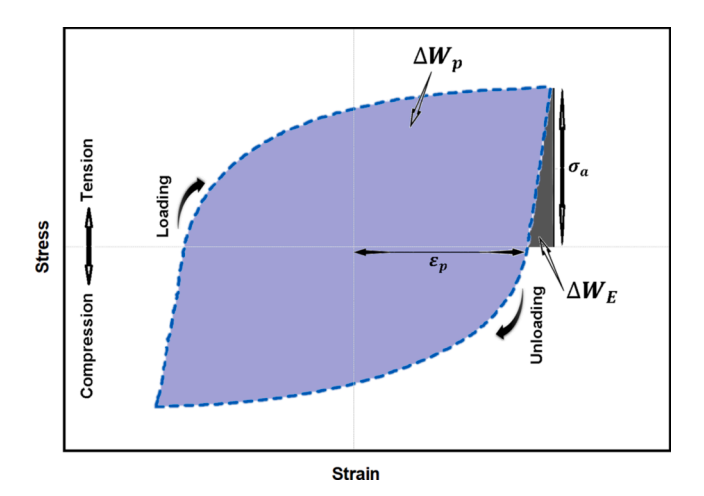
Prithivirajan and Sangid [19], who simulated the effect of manufacturing pores in the fatigue life of AM IN718 specimens via Crystal Plasticity Finite Element Modeling (CPFEM). Molaei et al. [20] studied the fatigue life of Laser Powder Bed Fusion (L-PBF) additively manufactured Ti-6Al-4V. They utilized the concept of extreme value statistics (EVS) to approximate the largest defect's effective size and predict fatigue life accordingly. Ziolkowski et al. [21] analyzed SS 316 samples fabricated with Selective Laser Melting (SLM) via X-ray computed tomography (XCT). They indicated that the porosity content in the horizontally-printed specimens is more than the vertically-printed and the angled ones. In contrast, the vertically-printed ones contained more porosity than the angled ones. Lee et al. [13] investigated the effect of intrinsic surface roughness (SR) in as-built L-PBF Ti-6Al-4V specimens vs machined/polished specimens, and introduced an SRbased parameter for the non-destructive fatigue life prediction of AM samples (where removing surface roughness via post-processing prior to testing is not desired).

The movement and transformation of microstructural defects under cyclic loading in low- and high-cycle fatigue (LCF and HCF)) regimes result in irreversible damage. The associated energy with the irreversible cyclic damage—slip irreversibility— or microplastic strain energy must be appropriately evaluated to represent the local sites of fatigue damage accumulation and crack nucleation [1,22]. Chun-Yu Ou et al. [23] calculated the plastic strain energy (PSE) at the potential sites for crack nucleation in AM Nickel-based super alloy (such as gaseous pores, lack-of-diffusion spots, and slip bands) to predict the fatigue crack

E-mail address: Khonsari@lsu.edu (M.M. Khonsari).

^{*} Corresponding author.

Nomenclature K Hardening coefficient (MPa) n Hardening exponent Fatigue life (Cycles) N T Temperature (K) Slip direction s Standard deviation std V_k Internal variables Plastic strain energy per cycle (MJ/m³.cycle) W_{D} Yield limit of a macro-element (MPa) Y Strain of a micro-element ϵ_k Plastic strain ε_{n} σ Stress (MPa) Coefficient of std α υ Poisson's ratio Mean of strain μ Entropy generation rate (MJ/m³.cycle)



 $\label{eq:Fig. 1. Plastic strain energy based on the area inside the cyclic stress—strain hysteresis loop.$

initiation (FCI) life of AM specimens with different microstructures. Wilson et al. [24] developed a method using the integrated crystal plasticity eXtended Finite Element (CPXFEM), where cyclic damage during fatigue crack initiation and growth (FCI and FCG) were quantified based on the locally-stored strain energy. They indicated that there is a strong correlation between the sites of the damage accumulation and the locations with maximum locally stored strain energy. Using the crystal plasticity finite element (CPFEM), Bandyopadhyay et al. [25] developed a statistically-based method to estimate the total microplastic strain energy in a cyclically-loaded medium. They concluded that the strain energy until failure is a property of the material. Douellou et al. [26] estimated the cyclic dissipated heat during the fatigue testing of L-PBF 18Ni300 and L40 steels using thermography techniques. They proposed a mathematical model for calculating dissipation at different stress levels. The interested reader may refer to a recent review of the relevant studies for the microstructure-sensitive quantification of fatigue damage and life [1].

AM processes provide opportunities to manufacture highly complex parts in various metallic alloys that are customized for specific working conditions, such as elevated temperatures. High environmental temperature conditions in components of aircraft engines, combustion chambers, and boilers in powerplants are examples of these environments [27]. Yet there is a paucity of easy-to-implement microstructure-sensitive methodologies for measuring fatigue damage at elevated temperatures, particularly with AM materials. Zhang et al. [28] used the cyclic stress–strain hysteresis loop (HL) energy to analyze the fatigue damage mechanism and obtain the fatigue life of MarBn martensitic steel used in the boiler and turbine parts of USC power plant at high temperatures. Zhang et al. [28] used the data and proposed a correlation between PSE and fatigue life for MarBn steel at different temperatures. Popovich et al. [29] studied the thermomechanical fatigue behavior of Inconel 718 additively manufactured via L-PBF technology. They observed that the fatigue lives of the specimens with larger grain sizes were lower than the ones with smaller grain sizes.

AM L-PBF Copper-alloys, specifically GRCop-42, GRCop-84, C18150, C18200, are of particular interest for various industrial and aerospace components [30–32], specifically for high heat flux applications such as combustion chambers [33,34]. Many of these alloys have been studied for use in the mentioned applications and examples are provided across the literature [35,36], but limited data is publicly available on their fatigue at elevated temperatures. Further, the majority of reports are on the simple tensile behavior [37,38]. Wegner et al. [6] studied the CuCzCr alloy processed with L-PBF and found that although the influence of processed-induced defects (pores and LOFs) is marginal on the alloy's failure behavior under simple monotonic tensile load, they were the main contributor to the nucleation of fatigue cracks. Jahns et al. [39] investigated the microstructure, relative density, and electrical conductivity of the AM CuCzCr alloy processed with L-PBF and gas atomization.

In this study, we estimate the fatigue damage and life of C18150 (Cu-1.5Cr-0.5Zr, wt.%) copper alloy AM specimens at the room (RT) and elevated environmental temperatures based on cyclic stress-strain hysteresis loop analysis and a recently developed microstructure-sensitive framework for analyzing cyclic fatigue. The efficacy of the microstructure-sensitive algorithm for AM specimens at elevated environmental temperatures and also the applicability of FFE to such condition is investigated, for the first time, in this manuscript. In what follows, first, the theoretical background is presented in Section 2. Section 3 is dedicated to the details of the experimental work in this study, and Section 4 discusses the numerical procedure. In Section 5, the cyclic plastic strain energy results using the SEPSE model (statistical estimation of plastic strain energy) and the cyclic stress-strain hysteresis loop are presented. Also, the efficacy of Fracture fatigue Entropy (FFE) as a materials index for fatigue is investigated. Finally, the concluding remarks are presented in Section 6.

2. Theory

The strong correlation between PSE and fatigue damage is well-established [1]. One of the most common ways to calculate the macroscopic plastic strain energy is by measuring the area inside the stress—strain curve from a cyclic test [40–42] (See Fig. 1). During the unloading step, the elastic portion of the strain relaxes, and the rest exhibits irreversible behavior (ε_p). As seen in Fig. 1, the area inside the loop only contains the plastic strains, and thus the associated energy density with this area is the PSE. The greater the applied cyclic stress amplitude (σ_a), the larger the area inside the hysteresis loop, the more pronounced the PSE effects become.

Intrinsic dislocations are generated during the manufacturing of metallic alloys. Under cyclic loading, the permanent displacements of such microstructural defects result in irreversible mechanical degradations such as the decrease in the material's modulus of elasticity and reduction in rigidity [43]. The reversible deformations, however, root in the rocking movements of dislocation substructures known as kink

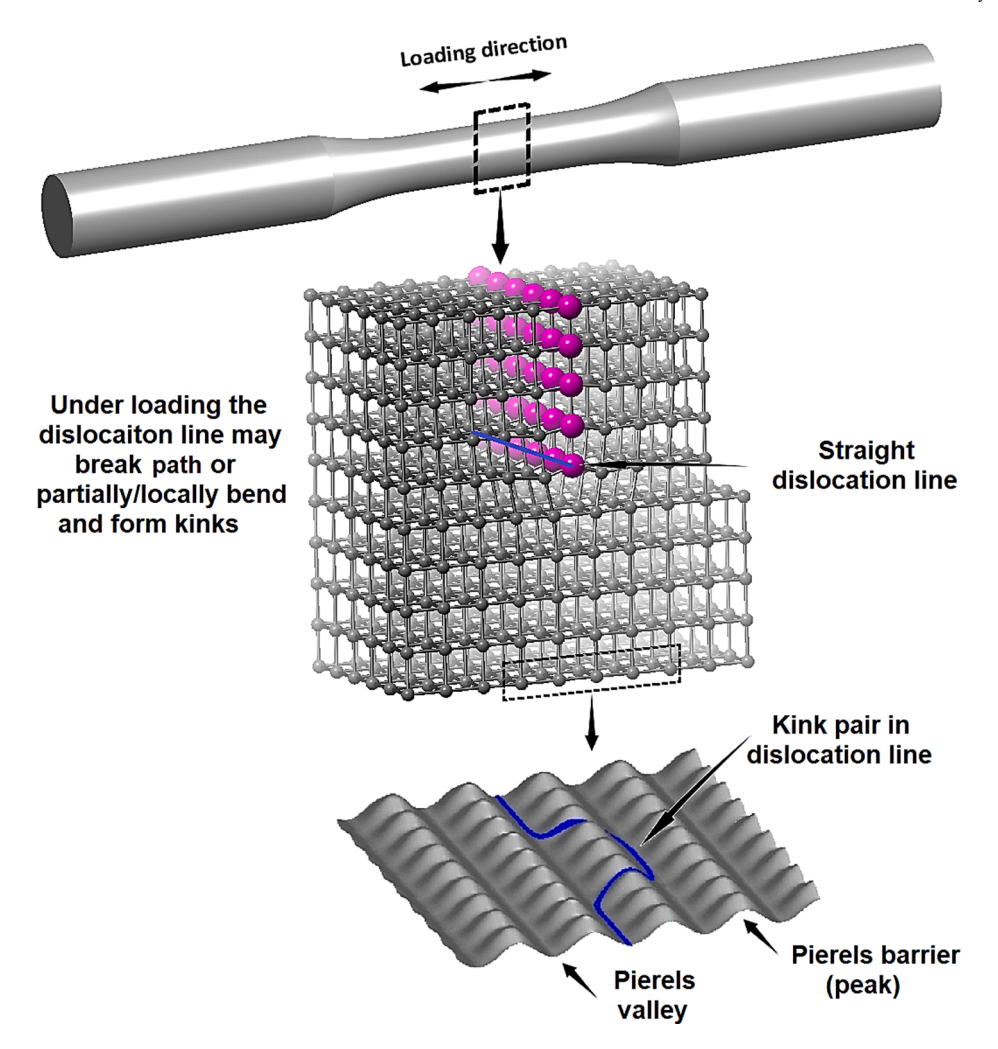


Fig. 2. Movement of dislocation structure (along the loading direction) in a cyclically-loaded specimen leading to reversible kink deformations that are associated with internal friction. The pink and grey atoms are all the same and only shown with different colors and sizes to differentiate between the half-plane of the edge dislocation and the full planes. (For interpretation of the references to colour in this figure legend, the reader is referred to the web version of this article.)

pairs¹ where they relax gradually by returning to their original equilibrium state, thus generating no plastic deformation (see Fig. 2). Such spring-like oscillations of the dislocation line are linked to the internal friction between a material's atoms or lattice friction [45–47] and reflect in the stress–strain hysteresis loop [48]. The non-damaging internal energy associated with this phenomenon is known as anelastic energy [48,49]. The size of the anelastic strain energy depends on the applied stress amplitude, frequency, and type of material [50].

Research shows that at fatigue lives starting at approximately above 60,000 cycles, the cyclic plastic strain inside a loop starts to partially recover [40]. The energy associated with the recovered strain from the loop is the same as the anelastic energy. Hence, in such cases, a cyclic stress–strain loop's internal area consists of both the damaging PSE and the non-damaging anelastic energy [51,52]. Wertz et al. [53] indicated that the size of the internal area of the hysteresis loop at a constant stress

amplitude increases monotonically with increasing the frequency up to 50 Hz, and related the increase to anelasticity. In other words, when the stress amplitude is kept constant and the testing frequency is increased, the plastic strain energy remains the same while the anelastic portion of strain energy enlarges [51,53,54]. However, throughout a fatigue test—at constant load amplitude and frequency—the amount of internal friction remains nearly constant before fracture [55]. Accordingly, Liakat and Khonsari [51] indicated that the area of the cyclic hysteresis curve in the early stages of a fatigue test (at around the 50th cycle after a servo-hydraulic fatigue tester has accomplished tuning) can be considered as the anelastic energy and evaluated this for testing frequencies up to 15 Hz. Liakat and Khonsari verified the proposed methodology via measuring the phase lag between the stress-time and strain-time in a fatigue test as a common method for finding the amount of internal friction [56,57]. Hence, in the present study, where the testing frequency is 10 Hz, when the hysteresis loop is used to calculate PSE per cycle, the non-damaging anelastic energy is subtracted from the loop area based on such a method.

Another approach to quantifying the PSE per cycle is the statistical estimation of plastic strain energy (SESPE) method [58]. The grain-level local micro strains in polycrystalline materials are highly inhomogeneous due to grain anisotropy and crystallographic orientation differences [59,60]. Based on the literature [61,62] microplastic strain distribution under cyclic and monotonic loads follow similar trends as shown in Fig. 3. Chen [61] investigated the distribution of cyclic von

Tire Kinks are the tiny deformations of dislocation lines that form without changing crystallographic planes when the same-type dislocations hit each other (screw-with-screw or edge-with-edge). A dislocation line breaks from its straight path and moves over a Pierel's peak once its potential exceeds the critical resolved shear stress. Although the single kinks, as such, lead to irreversible deformation, the thermally-activated double-kinks (kink pairs) are reversible since they move back to their previous path (previous equilibrium state or Pierel's valley as it can be seen in Fig. 2) and relax over time. Therefore, they can be associated with internal friction [44].

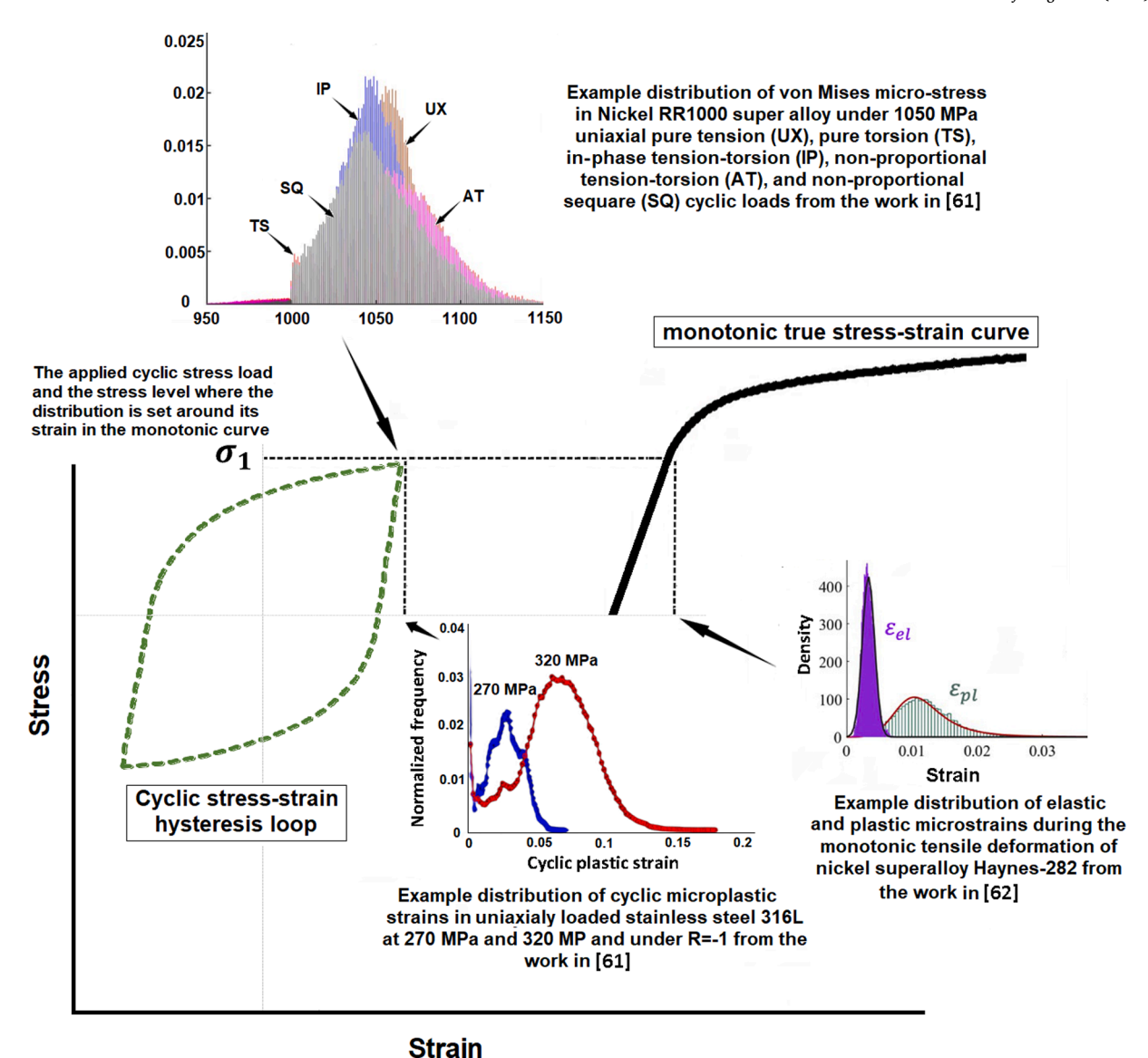


Fig. 3. A graphical presentation of the fundamentals for the SEPSE model based on the microplastic strain and stress distributions in a medium under monotonic [62] and cyclic loads [61]. The figure is just for the purpose of concept illustration and the numbers do not play a role.

Mises micro-stresses and micro-strains in a Nickle-base RR1000 super alloy under different uniaxial and multiaxial forms of loading. As shown in Fig. 3, Chen [61] indicated that the stress distribution follows a relatively Gaussian distribution, and the microplastic cyclic strains distribution contains a peak with a reduced frequency around the peak strain. Such an observation is understandable as a portion of the considered microelements do not undergo plastic deformation at the assessed loading amplitude. This is in agreement with the statistical distribution assumed by Jirandehi and Khonsari [58]. Hence the cyclic distribution of micro-strains can be approximated by a Weibull distribution function. Accordingly, the SEPSE method uses the true stress and associated true strain data points from a monotonic tensile test as distributed based on a two-parameter Weibull probability function $(f(\varepsilon) = \left(\frac{\varepsilon}{d}\right)^{r-1} e^{-(\varepsilon/d)^r}$, where *r* is the shape parameter and *d* is the scale parameter), to statistically acquire the PSE per cycle for an arbitrary cyclic stress amplitude (see Fig. 3).

In the SEPSE method, a polycrystalline material's microstructure is assumed in the form of heterogeneous elements with similar elastic moduli but different behavior in the plastic region. To this end, in this method, the micro elements with similar mechanical and

microstructural attributes are assigned with similar levels of plastic strain statistically. Note that the terms micro/meso/macro elements were introduced in the original work to illustrate the physics behind the proposed derivations. There are no real elements as such involved in the analysis. Locations within the microstructure where a bunch of juxtaposed grains with the same spatial orientation and slip characteristics exist are identified as potential sites of crack initiation under fatigue [63]. However, it is important to consider that only the elements that align with energetically-favorable slip systems surpass the critical resolved shear stress under loading and experience yielding. Considering that the strain experienced by any element in a polycrystalline agglomerate has five components (excluding the hydrostatic term), the microscopic elements need to multi-slip in at least a set of five independent slip systems (s) [64]. Accordingly, Esin and Jones [65] put forward a probability function ($f(s) = \sum_{i=1}^{5} \frac{1}{2s-(i-1)}$) that considers the least number of slip systems required for the deformation to occur and also preserve material's continuity. Therefore, the contribution of one element to the total PSE accumulated in one cycle is derived based on Eq. (1), where the *flow rule* is used to include the hardening effect ($\sigma =$ $K\varepsilon^n$).

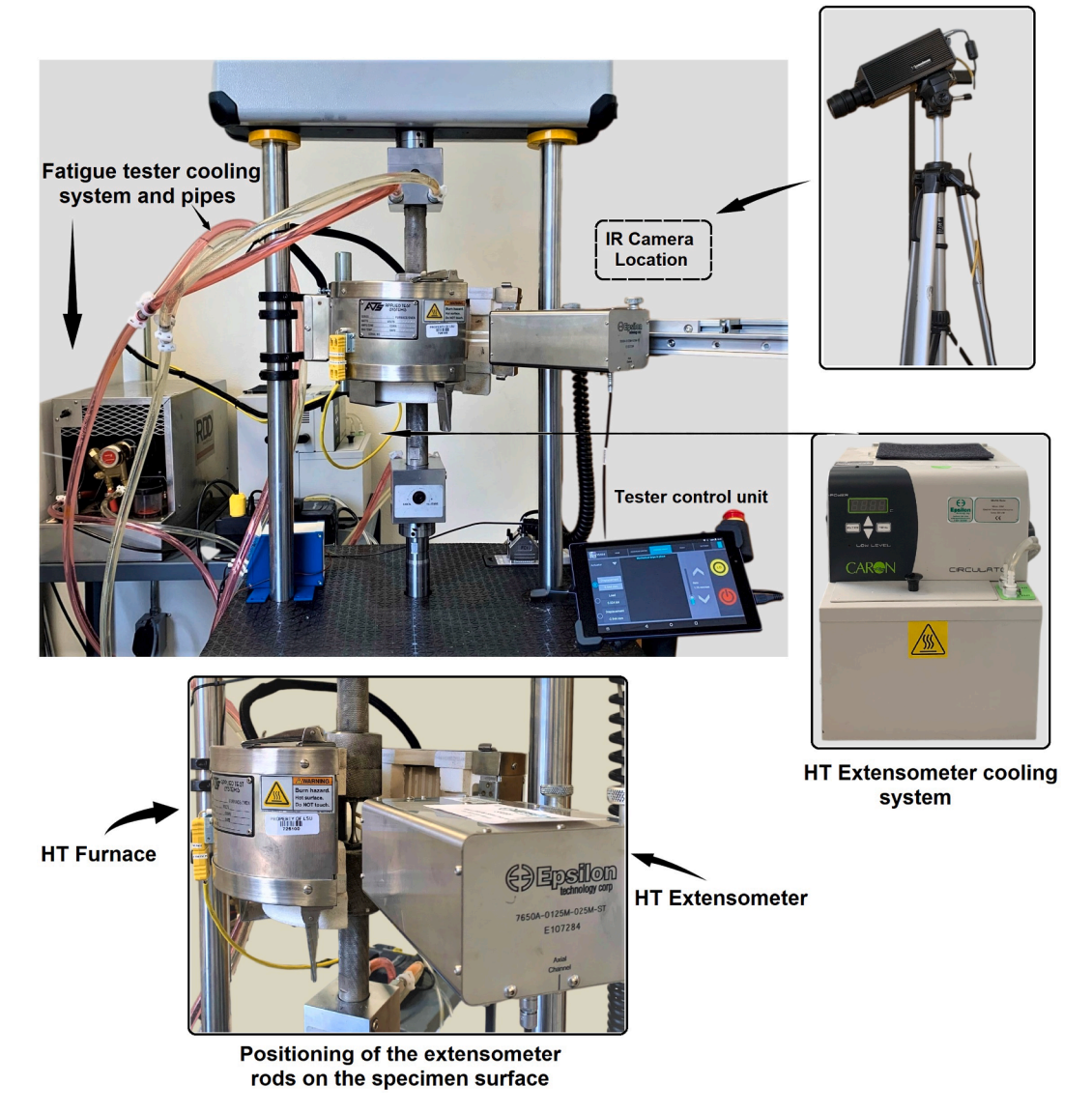


Fig. 4. The experimental setup used to conduct the fatigue experiments in this study.

Table 1The fatigue tests load amplitude and environmental temperatures in this study.

	1				1		
Stress Amplitude (MPa)	100	110	115	120	125	130	135
Temperature (°C)	RT, 204, 426	RT	204, 426	RT, 204	RT, 204	RT	RT

$$dE = 2 \sigma f(s) f(\varepsilon_p) d\varepsilon_p$$

$$= 2 \left(\sum_{i=1}^{5} \frac{1}{2s - (i-1)} \right) K \varepsilon_p^n \underbrace{\frac{\alpha \times std}{\mu}}_{\text{scale parameter}} \left(\frac{\varepsilon_p}{\mu} \right)^{\alpha \times std - 1} e^{-\left(\varepsilon_p/\mu\right)^{\alpha \times std}} d\varepsilon_p \qquad (1)$$

where σ is an element's micro-stress, ε_p is an element's microplastic strain, K is the hardening coefficient, n is the hardening exponent, μ is the average of the strain datapoints distributed with a Weibull function around the peak strain associated with σ_1 in Fig. 3, and std is the standard deviation of the selected data points for a particular load amplitude.

From the assigned statistical distribution of micro strains $(f(\varepsilon))$ a

portion of the elements as represented by the area under the Weibull density function curve starting from the true yield point experience plasticity (the interested reader may refer to [58] for detailed discussion. After setting the limits of integration, the distribution of cyclic microplastic strains becomes similar to that indicated in Fig. 3). Consequently, Eq. (1) can be rewritten in integral form for all of the statistical elements (*k*) to calculate the PSE per cycle based on the normalized frequency of plasticized elements.

$$W_{SEPSE} = \sum_{i=1}^{k} 2K \frac{\alpha \times std}{\mu^{\alpha \times std}} (\sum_{i=1}^{5} \frac{1}{2s - (i-1)}) \int_{\gamma}^{\epsilon_{k}} \varepsilon_{p}^{n + \alpha \times std - 1} e^{-(\epsilon_{p}/\mu)^{\alpha \times std}} d\epsilon_{p}$$
 (2)

where k is the number of statistical elements, Y the true yield strain point, and s is the number of slip systems based on the material's microstructure, and α is the coefficient of standard deviation. A proper value α occurs at the point where $\frac{\partial^2 PSE}{\partial \alpha^2} = 0$ and where the Weibull peak strain corresponds to the associated strain with σ_1 in Fig. 3 [58]. The merit of the SEPSE method lies in using monotonic tensile test data (including constants such as K and n) in conjunction with the functions that represent material's behavior under cyclic loading. Although using the strain hardening exponents and coefficients from the monotonic test

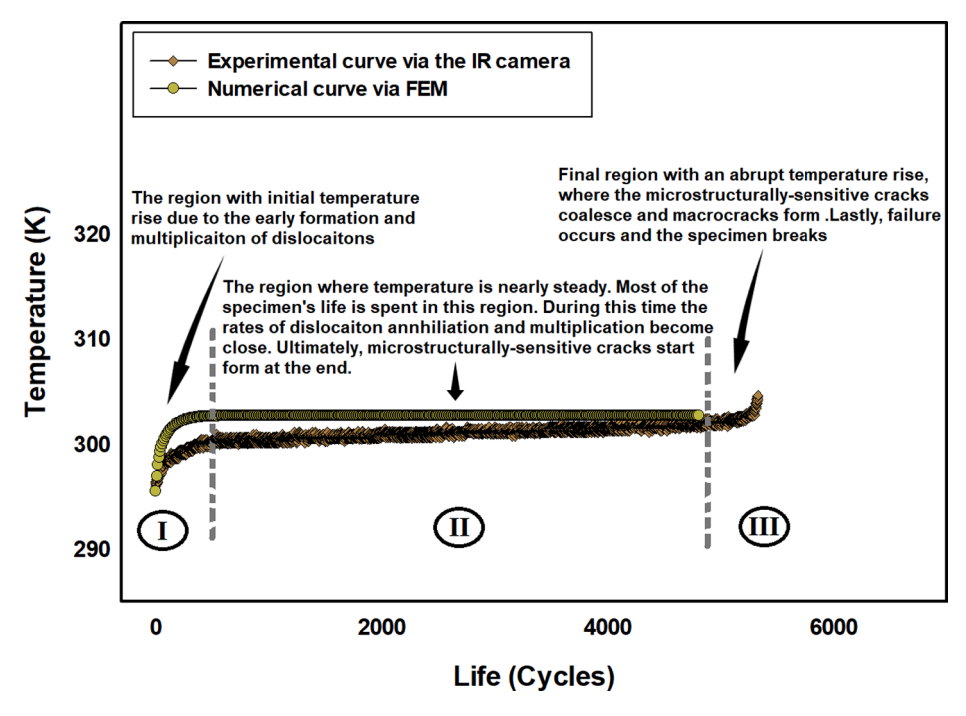


Fig. 5. temperature evolution of the specimen under 135 MPa cyclic load with 10 Hz frequency (R = -1) via the IR camera measurements and finite element analysis. The steady-state temperature from Stage 2 is used to calculate the FFE via two approaches.

Table 2
Thermal properties of the L-PBF C18150 copper alloy at different temperatures
[72]

[/ 2].			
Temperature (°C)	$C_p \left(\frac{J}{Kg.K} \right)$	k (W/m.K)	
Room Temperature	385	110	
204	400	137	
426	400	260	

data may introduce small error of estimation with some materials, based on our experience, its application yields satisfactory results and outweighs the disadvantages of very complex models. During a fatigue test, plastic strain energy is generated in the specimen's gauge section and is converted into heat. Part of this heat contributes to increasing the material's temperature $(\sigma: \dot{\varepsilon}^p)$ and the other part is conducted to the machine's grips $(k\nabla^2T)$ [51,66]. When the principle of conservation of energy is implemented, one can arrive at the following heat transfer equation [67].

$$\rho C \dot{T} = \dot{w_p} + k \nabla^2 T \tag{3}$$

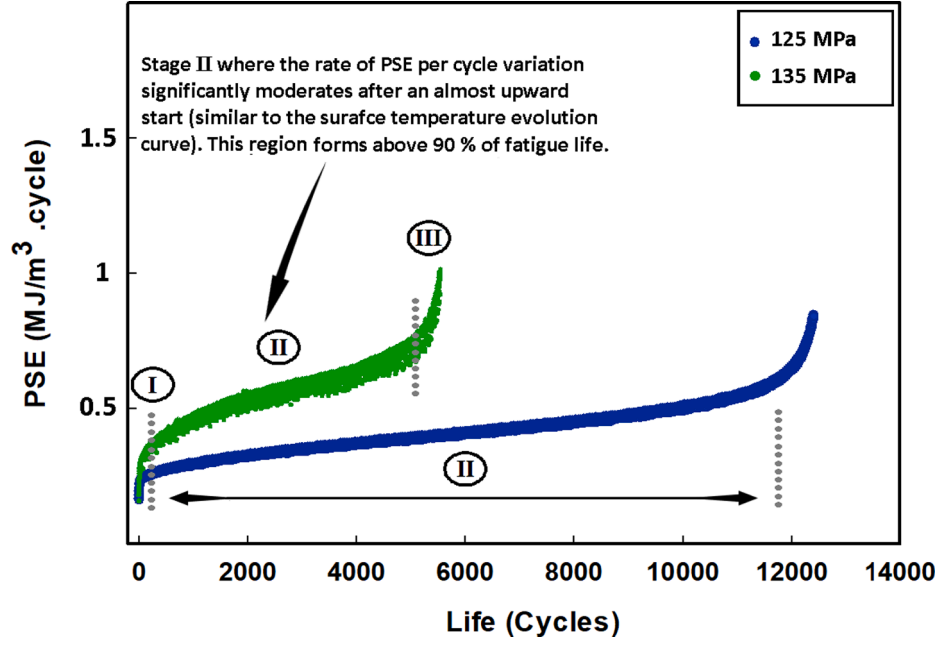


Fig. 6. HL internal area evolution for $\sigma=125$ MPa and 135 MPa at RT.

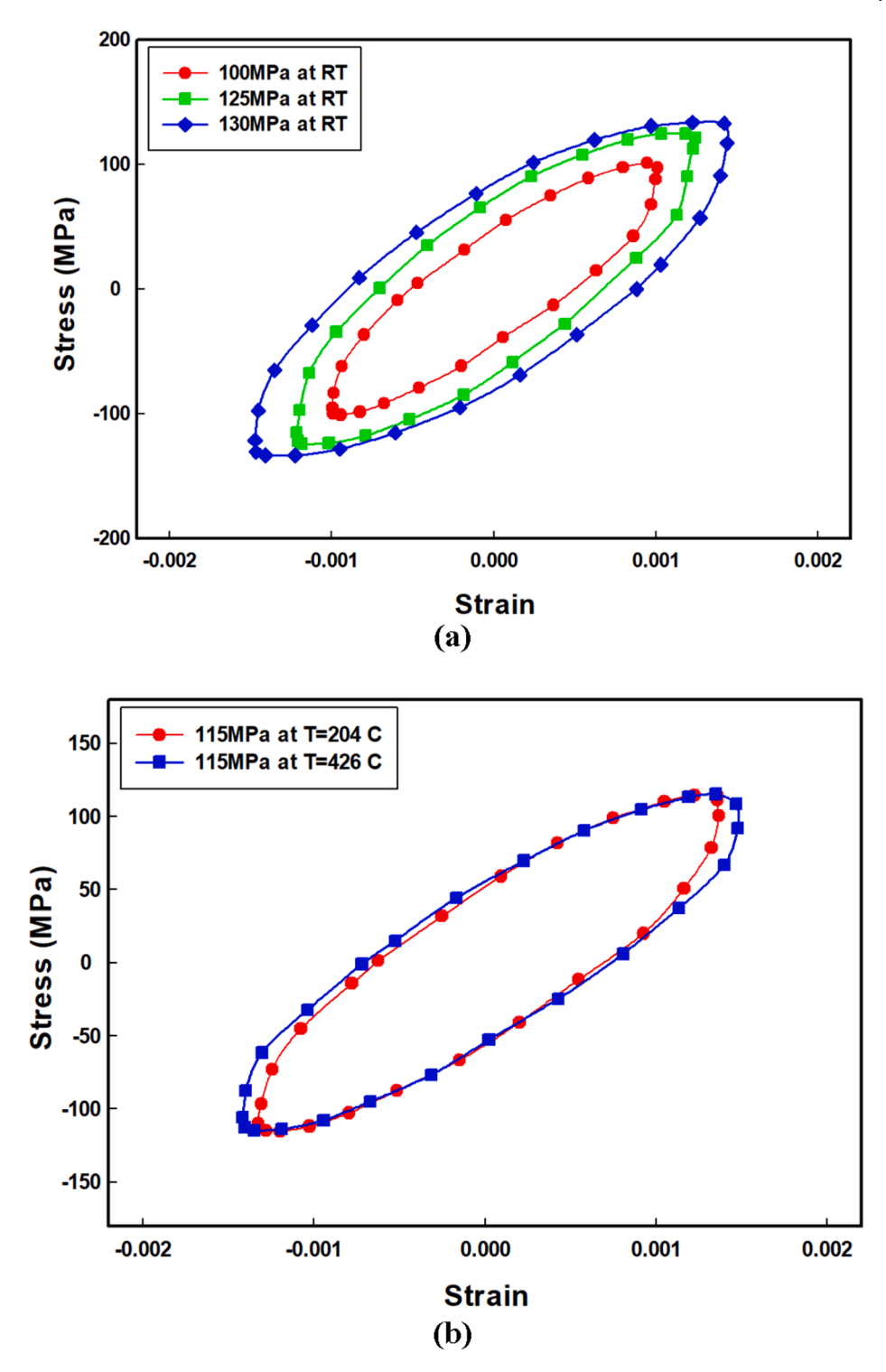


Fig. 7. Hysteresis loop evolution after 500 cycles and with a) increasing the stress amplitude b) increasing the environmental temperature at a constant stress amplitude (all the loops are shifted to the center of the coordinates to visualize the relative behavior).

where $\dot{w_p} = \sigma$: $\dot{\varepsilon}^p$ represents the PSE rate, ρ is the material's density, and k is the thermal conductivity.

The second law of thermodynamics in the form of Clasius-Duhem inequality $(\rho \frac{\partial s}{\partial t} + \nabla \cdot (\overrightarrow{q}_T) \ge 0)$ can be used to obtain the rate of volumetric entropy generation $(\dot{\gamma})$ in the gauge section of a test specimen [68].

$$\dot{\gamma} = \frac{1}{T} \left(\sigma : \dot{\varepsilon}_p - A_k \dot{V}_k - \frac{k \nabla^2 T}{T} \right) \ge 0 \tag{4}$$

where $\sigma:\dot{e}_p$ is plastic strain energy and equals the \dot{w}_p term in the Eq. (3), the second term is the nonrecoverable stored energy, and the third term is the dissipated heat through conduction [67]. Considering the dominance of the first term in Eq. (4), the accumulation of the produced entropy over the life of the specimen until final failure (t_f)—known as the Fracture Fatigue Entropy (FFE)—can be obtained via the Eq. (5) [66,68]. Research shows that FFE is independent of geometry, load, and frequency [69–71].

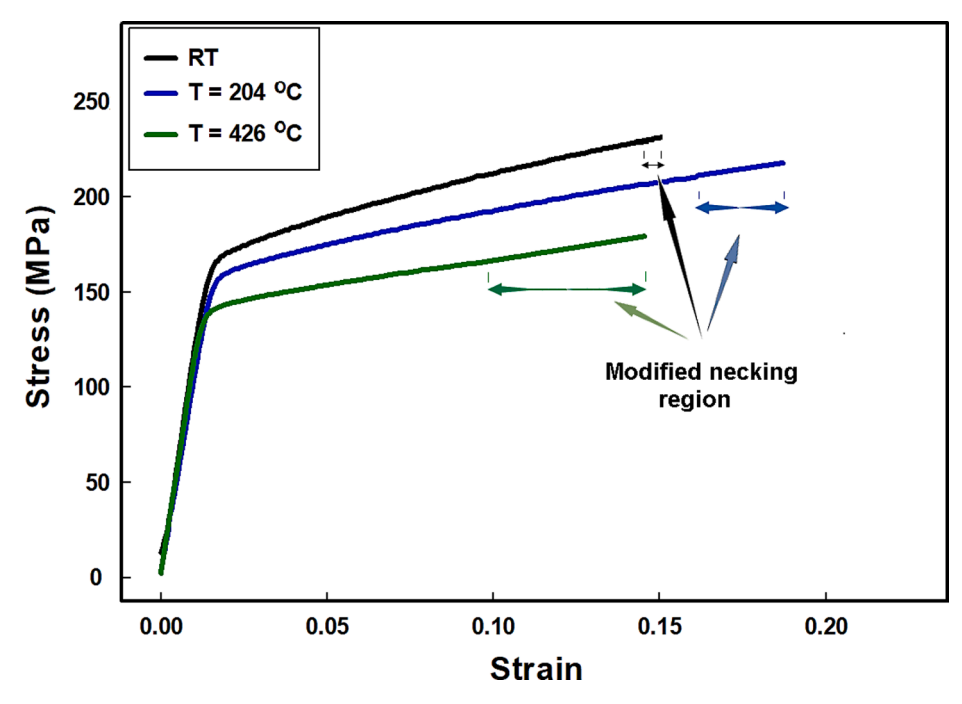


Fig. 8. The true Stress–strain curve of the additively manufactured C18150 copper alloy used in this study at RT, T = 204 °C, and T = 426 °C. In the modified necking region the post-hardening part of the curve is linearly approximated with the slope of the hardening region.

Table 3The mechanical properties of the additively manufactured C18150 copper alloy used in this study.

Temperature	Density $(\frac{kg}{m^3})$	True Yield (MPa)	Ultimate Strength (MPa)
Room Temperature	8900	120	200
$T=204~^{\circ}C$	8900	115	180
$T=426\ ^{\circ}C$	8900	100	150

$$FFE = \int_0^{t_f} \dot{\gamma} dt = \int_0^{t_f} \frac{\dot{w}_p}{T} dt \tag{5}$$

where T is the surface temperature of the specimen. It is typically measured via an IR camera during the experiment. Alternatively, it can be estimated using the finite element method (FEM) and discretizing the Eq. (3) over the domain of the specimen. After finding the FFE of material via Eq. (5) or its simple form in Eq. (6), the same equation can be used to estimate the fatigue life for an arbitrary load amplitude.

$$(FFE = \frac{N_f * \dot{w}_p}{T_{ex}}) \tag{6}$$

In brief, a full analysis with the SEPSE-based framework—including the FEM to obtain the steady-state temperature— requires conducting a simple monotonic tensile test to get the true stress–strain curve (hardening exponent and coefficient are also derived from this curve), the number of slip systems in the material, specific heat capacity, density, heat conductivity coefficient, and 2–4 cyclic tests just to obtain fatigue life (4 is a conservative measure and ensures a good average of FFE [67]).

3. Experimental

A servo-hydraulic fatigue tester (Test Resources-910 series) with a maximum capacity of 25 KN load and 60 Hz frequency is used to perform uniaxial cyclic and monotonic tests. In this setup, specimens are gripped between the bottom and top jaws, where the top jaw stays stationary,

and the bottom jaw oscillates (See Fig. 4).

Argon atomized C-18150 spherical powders with d10, d50, d90 sizes at 19 $\mu m, 29.1~\mu m,$ and 45 $\mu m,$ respectively, are used as raw materials (Praxair Surface Technologies, Indiana, USA). Cylindrical rods are fabricated using the L-PBF process in a vertical orientation (Z-height) from C-18150 (Cu-1.5Cr-0.5Zr, wt.%). Cylindrical dog-bone specimens used in this study are designed and machined in accordance with the ASTM E466-15 standard. The gauge section of all of the fabricated specimens is polished using silicon carbide sandpapers with grit numbers ranging from 400 to 3000 to achieve a maximum surface roughness of 0.2 μm . This step was taken to ensure that the existing surface roughness in as-built specimens is eliminated and does not affect the fatigue test results. The specimens used in this study have received no heat-treatment/aging prior to testing.

A high-temperature furnace (Test Resources-F1000 series) and a temperature control subsystem were used. The furnace can heat up to 900 $^{\circ}$ C and the maximum temperature can be reached in less than 30 mins. The short time range for heating up ensures that the specimen is minimally affected by the heating it receives prior to testing and has enough time to reach a uniform temperature at all the spots along its gauge section. In addition, a water-based cooling unit is responsible for preventing the fatigue jaws from overheating.

A high-temperature high-precision extensometer (Epsilon, Model 7650A) is used to record the cyclic strain response at both the room and high-temperature operating conditions. The extensometer can measure strain at fatigue tests with up to 10 Hz frequency and environmental temperatures of up to 900–1200 °C. Precision rods/blades made of high-purity alumina contact the test specimen's surface enabled us to perform safe and accurate measurements at a broad operable temperature range. The extensometer is constantly water-cooled via a bath circulator (Caron, model-2050) during the tests to maintain the optimal performance of its electrical units. The extensometer is installed on a standalone setup. It is separate from the fatigue tester to eliminate any potential effect of frame vibration on the measurements (See Fig. 4).

Monotonic tensile tests are conducted at three environmental temperatures of room, 204 $^{\circ}$ C, and 426 $^{\circ}$ C to obtain the stress–strain curve. All fatigue tests are conducted under 10 Hz frequency and at a combination of stress levels and environmental temperatures to best capture

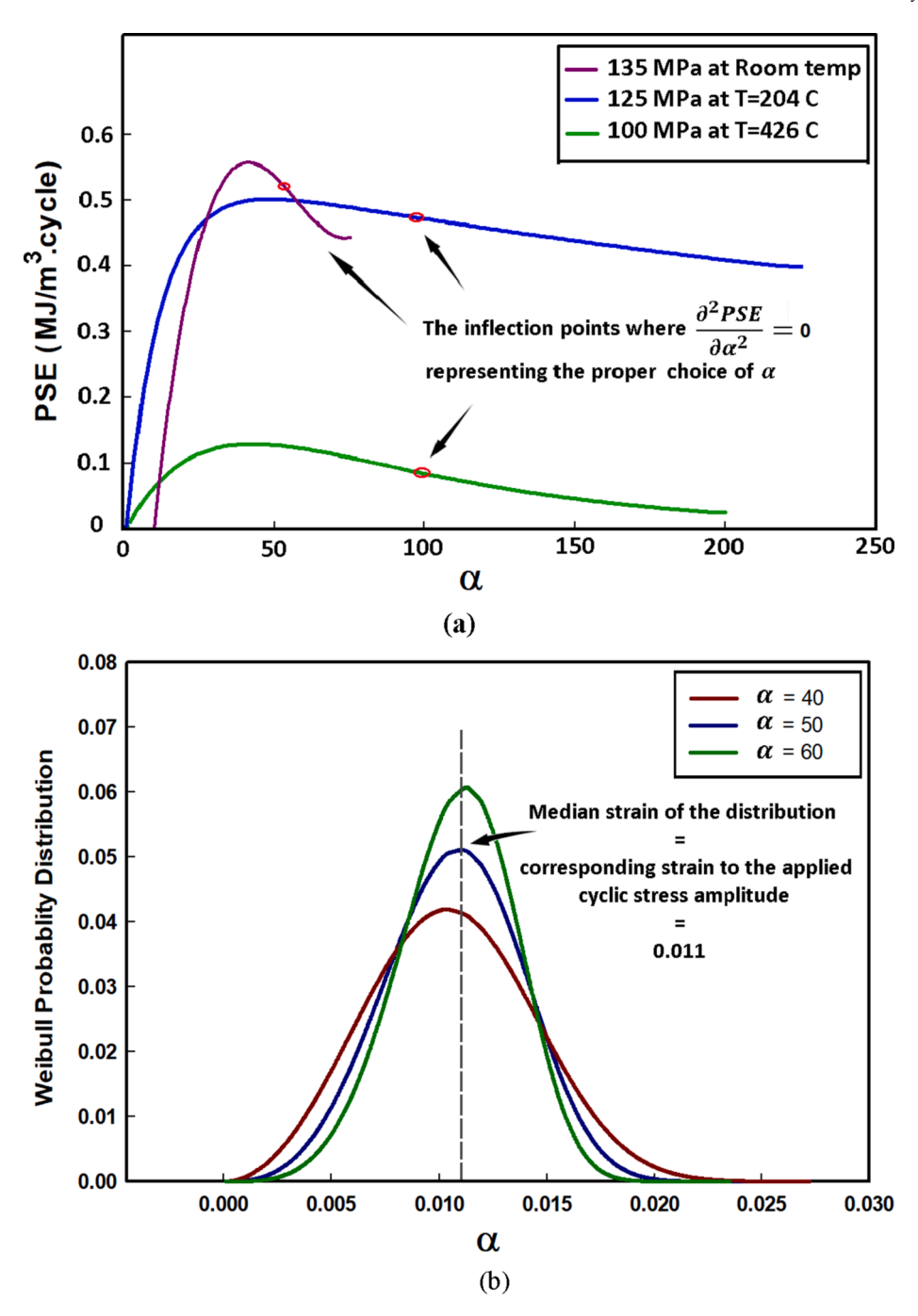


Fig. 9. The SEPSE model procedure for the determination of the α parameter a) the variation of PSE with α for $\sigma = 135$ MPa at RT, $\sigma = 125$ MPa at T = 204 °C, and $\sigma = 100$ MPa at T = 426 °C b) the Weibull distribution for different α values at 135 MPa and at RT.

the change in behavior with a change in either of the stress and temperature elements. Specifically, the stress levels/temperatures tested are listed in Table 1.

4. Numerical

The thermodynamics of solids has been widely implemented to arrive at parameters and develop methods that can quantify fatigue characteristics and predict the useful life of metals by analyzing the energy dissipation during cyclic fatigue [1]. To use Eq. (6) to calculate a material's FFE, the temperature signature of the metal under cyclic loading is required. When experiments are conducted at room temperature (RT), the temperature signature can be obtained both experimentally via the installed IR camera (Fig. 4) and predicted numerically

via FEM. However, when the furnace is closed and the experiments are performed at elevated temperatures, only the verified developed FEM can calculate the temperature evolution reliably.

The temperature evolution of a specimen under cyclic loading follows three stages [67] (See Fig. 5). The temperature evolution curve throughout the fatigue life cycle of a specimen is similar to that of the hysteresis stress–strain curve. In Stage I—the first few cycles in the early stages—the specimen's surface temperature rapidly increases due to the formation of dislocations. In stage II the temperature evolution becomes steady since the rate of dislocation annihilation and multiplication become close and continue for most of the specimen's life. When calculating FFE based on Eq. (6), the steady-state temperature from the second stage is used. Lastly, in Stage III, the dislocation density increases rapidly due to an increase in multiplications, micro-cracks coalesce into

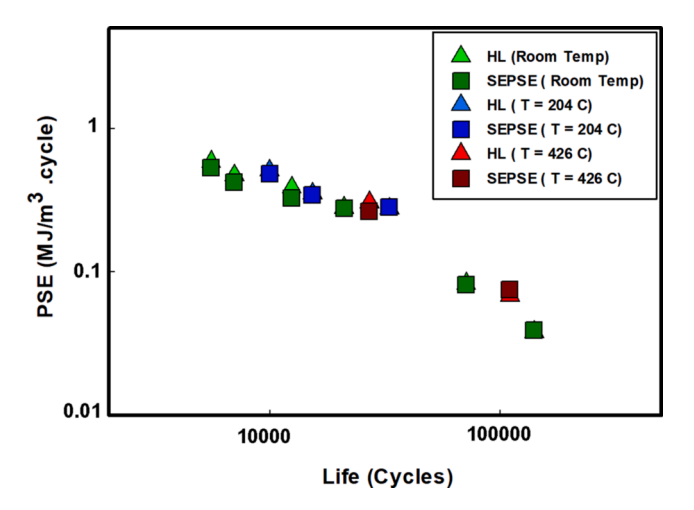


Fig. 10. The PSE values via calculating the area inside a hysteresis loop and the SEPSE method for $\sigma=100$ MPa (RT, 204 °C, and 426 °C), 110 MPa (RT), 115 MPa (204 °C, and 426 °C), 120 MPa (RT, 204 °C), 125 MPa (RT, 204 °C), 130 MPa (RT), and 135 MPa (RT). PSE is shown in terms of the volumetric plastic energy generated in one cycle.

a macro crack(s) that rapidly propagates, and specimen fractures. This stage of the fatigue life is very short, and it manifests itself in the form of a rapid rise in temperature just before fracture.

A finite element code developed by the authors in the Mathematica software environment was utilized to predict the evolution of surface temperature [67]. Since the environmental temperature varies in the experiments conducted in this study, the temperature-sensitive thermal properties and the associated coefficients must be carefully chosen for each environmental testing temperature. For this purpose, the measurements of specific heat and thermal conductivity of C18150 copperbased alloy reported in Table 2 are used [72].

5. Results and discussion

5.1. Hysteresis loop evolution and plastic strain energy

Research indicates that after the abrupt change in the size of the hysteresis loop (after the first few cycles), the plastic strain energy experiences minimal/moderate changes for the majority of fatigue life until it reaches a final stage before failure, where it sees a rapid increase again [25,73,74]. Fig. 6 shows the hysteresis loop energy variations over time for $\sigma=125$ MPa and 135 MPa at RT. In particular, the abrupt expansion in the hysteresis loop internal area early in the test relatively moderates, in the same way that the temperature variation moderates once it reaches stage II in Fig. 5 (since both the temperature and the HL are indicatives of heat dissipation). Considering that the majority of life (well over 90 percent- see Figs. 5 and 6) is spent in stage II and this stage itself sees (at worst) a moderately linear variation (despite all the cyclic hardening/softening at room/high temperatures) it is viable to consider the average PSE value of this region for the estimation of total plastic strain energy until failure

With increasing the cyclic stress amplitude, the magnitude of the cyclic PSE (the area contained within the hysteresis loop) is expected to increase [43]. Fig. 7-a shows the change in the hysteresis loop size with increasing the cyclic stress amplitude. It is also known that with increasing the environmental temperature at a fixed cyclic stress amplitude, the hysteresis loop is expected to increase. Physically, the added temperature boosts the kinetic energy of dislocations and results in added movements, which manifests in the form of added strains due to cyclic softening, and the hysteresis loop area becomes larger. Referring to Fig. 7-b, it can be seen that although the stress level is the same, at 426 °C the recorded strain is increased compared to the case of the test

conducted at 204 °C.

Research shows that the summation of the time spent in Stage II of hysteresis loop evolution (where the slope of hysteresis loop size variations moderates), by far, exceeds the two stages before and after Stage II; i.e. the first and third stage account for less than 10% [51,74,75]. This trend resembles the evolution of a specimen's surface temperature under cyclic loading, where the cyclic dissipated heat appears in the form of temperature rise during three main stages [67]. Hence, it is viable to assume that the plastic strain energy remains stable for the majority of the specimen's fatigue life [67].

To calculate the PSE per cycle in this work, several loops in the midlife region (Stage II) in each loading case are chosen, and the average hysteresis area is used as the associated PSE per cycle. Such an averaging method is adopted to arrive at a PSE value that best represents the stabilized stage of the hysteresis stress–strain curve (or the Stage II of the surface temperature evolution curve). As explained in Section 2, for the cases where the fatigue life exceeds 60,000 cycles, the HL area at around 50th cycle is used as the anelastic energy for that case and subtracted from the mid-life PSE per cycle (all of the fatigue tests are performed under constant amplitude and frequency).

Additionally, a recent microstructure-sensitive algorithm for the determination of cyclic damage known as SEPSE (as explained in Section 2) is used to determine the PSE per cycle. The SEPSE method uses the strain and the associated stress data points from a monotonic tensile test and the material's slip systems information to quantify cyclic PSE based on Eq. (2). Hence, the true stress–strain curves of the studied material at the three environmental temperatures are required.

Fig. 8 and Table 3 show the monotonic tensile stress–strain curve and the mechanical properties of the C-18150 copper alloy in this study at RT, T = 204 °C, and T = 426 °C. The density of the samples was measured based on the Archimedes method and reported in a prior study [72]. The true yield limits were determined from the stress–strain curves in Fig. 8 and at the point where the stress–strain curve becomes nonlinear. The ultimate strength values were merely identified as the point of maximum stress for each of the curves in Fig. 8. Additionally, the slope and abscissa of the logarithmic true stress–strain in the hardening region were used to experimentally determine the strain hardening exponent and coefficients ($\sigma = K\varepsilon^n \rightarrow \log \sigma = \log K + n \log \sigma \varepsilon$). The strain hardening exponents and coefficients at RT, T = 204 °C, and T = 426 °C were n = 0.15, 0.14, and 0.1, and K = 303 MPa, 266 MPa, and 205 MPa, respectively.

The approximated plastic strain energies via SEPSE are sensitive to the value of the shape parameter in the Weibull probability function [58]. Since the shape parameter is defined as the coefficient α multiplied by the standard deviation of the data points chosen around the applied cyclic load [58], an analysis is performed to find the proper α values for each of the load cases. By applying the procedure explained in Section 2 and considering the standards for obtaining the appropriate value of α for each case, values of PSE per cycle were obtained via the SEPSE. As seen in Fig. 9, for the example case of $\sigma=135$ MPa at RT, the second derivative of PSE change with α changes direction at approximately $\alpha=50$. It can also be seen that at this α value, one obtains a proper distribution of micro strains with the peak sitting at the strain value that corresponds to the applied cyclic stress amplitude.

Fig. 10 shows the calculated PSE values based on the measured area inside the hysteresis loops along with the estimated values via the SEPSE method for fatigue lives at the room, $204\,^{\circ}$ C, and $426\,^{\circ}$ C temperatures. It can be seen that for all of the measured fatigue lives in low- and medium-cycle fatigue regimes, the estimations via both of the methods are in close agreement. On the one hand, AM metallic specimens *generally* contain a large number of pores and a fair scattered distribution of pores from one specimen to another. Thus, a potential difference in mechanical properties among specimens is expected (The level of difference and its reflection on the mechanical properties related to the monotonic tensile test can be simply checked by repeating the tensile tests to ensure the scatter is insignificant). On the other hand, when using the SEPSE

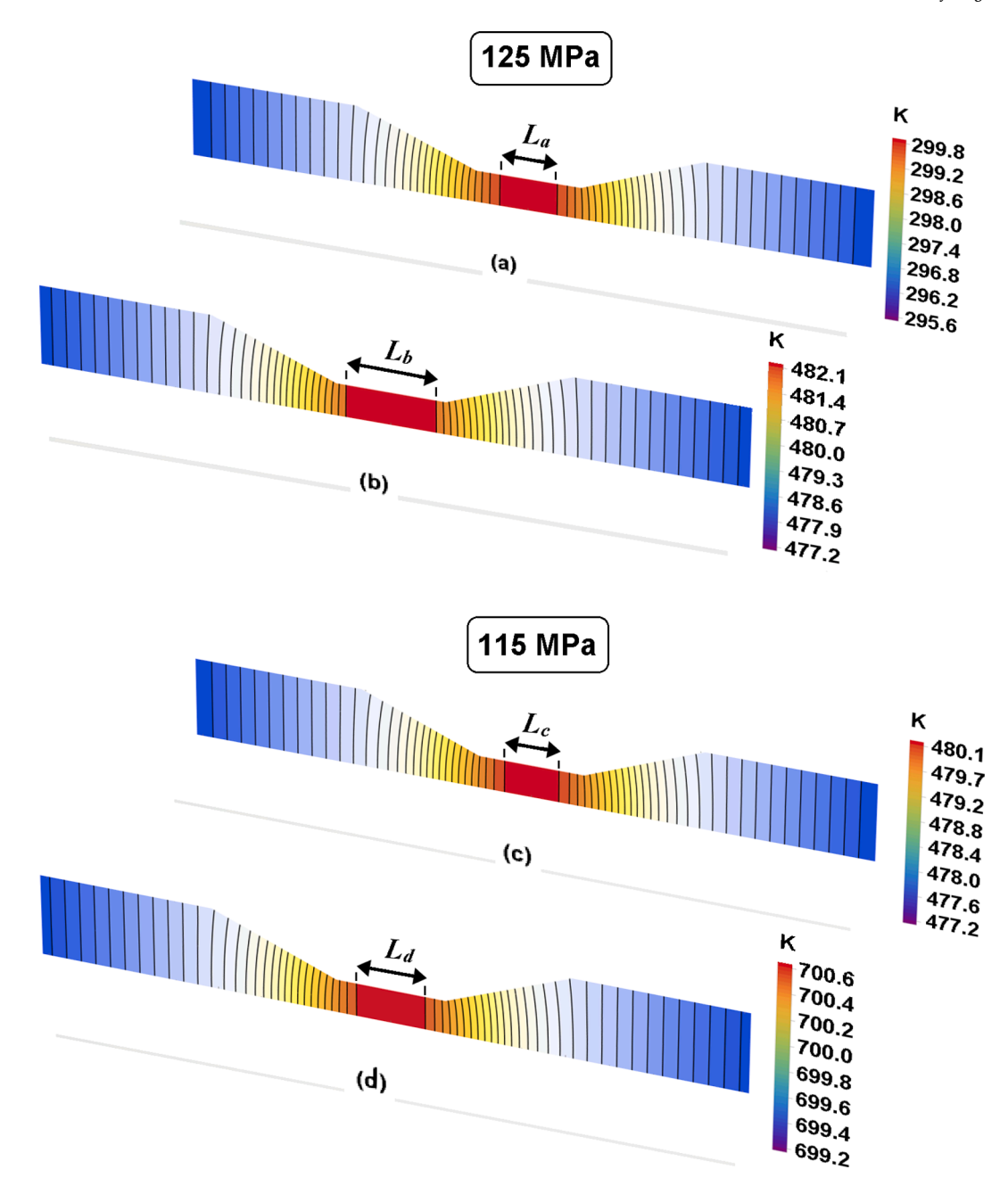


Fig. 11. The temperature distribution at different environmental temperatures for $\sigma = 125$ MPa at a) RT, b) T = 204 °C, and for $\sigma = 115$ MPa at c) T = 204 °C, d) T = 426 °C.

Table 4Thermal diffusivity of C18150 at different environmental temperatures [72]

Temperature	Room	204 °C	426 °C
Thermal diffusivity $(\frac{m^2}{s})$	32×10^{-6}	40×10^{-6}	70×10^{-6}

method, it is important that the monotonic stress–strain curve properly represents the specimens used for fatigue testing. If the property values are significantly different, the performance of the model will be negatively affected. Hence, the close agreement between the PSE results from the HL and the SEPSE method is a hypothetical indicative of the low porosity and good quality of the used AM C18150 specimens in this study (a previous study on the similar material have reported a much larger scatter in the tensile stress–strain curve across several samples

[76]). It is worthwhile to point out that the α parameter plays an important role in obtaining accurate results. If the scatter in the stress–strain curve of the samples from one batch is significant, then a correctly chosen alpha value based on the guideline or even changing alpha may not resolve accuracy issues.

5.2. Fracture fatigue entropy

To estimate the FFE, the surface temperature in Stage II or the steady-state temperature at each cyclic test is needed. To obtain the temperature signature of the specimen surface in Stages I and II, an IR camera was used to measure the steady-state value for the experiments conducted at room temperature. Then, the FEM is utilized to obtain the steady-state temperature for these load amplitudes and used along with the predicted plastic strain energies via SEPSE. Although the efficacy of the FEM is already demonstrated in [67], this measure was taken to

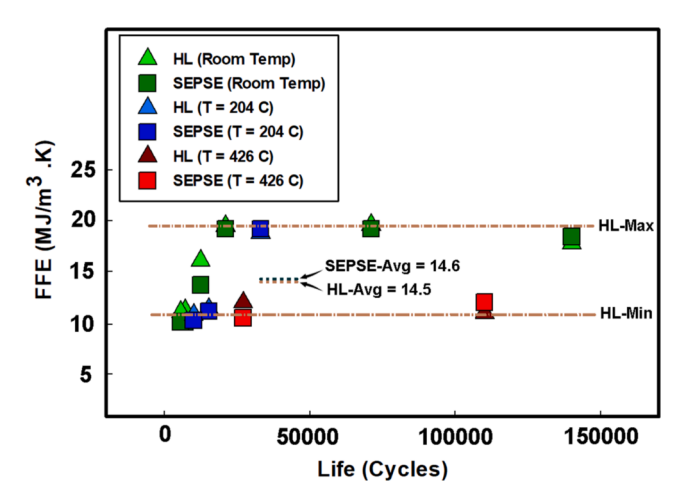


Fig. 12. The calculated FFE via the hysteresis loop measurements and the SEPSE estimations.

further ensure its accuracy for the current material. Having verified the numerical prediction, next, the FEM was used to calculate the temperature in Stage II for the experiments at high environmental temperatures, i.e., $T=204\,^{\circ}\mathrm{C}$ and 426 $^{\circ}\mathrm{C}$ (with both of the HL and SEPSE methods).

Fig. 11 illustrates the distribution of surface temperature on the specimen's surface with increasing the environmental temperature from RT to 204 °C at $\sigma=125$ MPa, and also from 204 °C to 426 °C at $\sigma=115$ MPa stress level. It can be seen that at higher temperatures, the length of the strip with critical temperature expands ($L_b > L_a$ and $L_d > L_c$). This behavior can be explained based on the change in the thermal diffusivity of this material at RT, T=204 °C, and 426 °C (see Table 4). Thermal diffusivity is indicative of a material's tendency to move heat from hot to cold regions. Thus, considering a cyclically-loaded cylindrical specimen, a higher thermal diffusivity means a higher tendency to transfer heat via conduction from the hot spots in the gauge section to the relatively colder regions in their vicinity [77]. Based on Table 4, the thermal diffusivity of C-18150 increases when the environmental temperature is increased. Therefore, at higher temperatures, the length of the region with the highest temperature increases.

Using the microstructure-sensitive algorithm for the estimation of FFE—where SEPSE is used to estimate cyclic damage in terms of PSE per cycle-and the cyclic HL area, the values of FFE for different stress amplitudes and environmental temperatures are calculated. From Fig. 12 it can be seen that the values of FFE fall within the indicated range irrespective of the stress amplitude and environmental temperature (HL-Max = 19.7 $\frac{MJ}{m^3.K}$ and HL-Min = 10.5 $\frac{MJ}{m^3.K}$). Importantly, the average value of FFE based on the experimental measurements of the hysteresis loop area (14.5 $\frac{MI}{m^3 \cdot K}$) are very close to the value calculated with the SEPSE- based algorithm (14.3 $\frac{MJ}{m^3.K}$). Such correspondence further attests to the reliability of the microstructure-sensitive framework put forward in [67] for the fatigue damage assessment of additively manufactured specimens. The SEPSE-based microstructuresensitive algorithm used for the fatigue damage quantification and life estimation of the C18150 is not dependent on the fracture mechanism. All of the microstructure interactions under cyclic loading gradually and accumulatively manifest in the form of local plastic micro-deformations or cyclic slip irreversibility. As explained in Section 2 of this manuscript, it is experimentally observed and established that the distribution of cyclic plastic micro-strains can be represented with a Weibull probability distribution function. With that in mind, the algorithm uses the associated energy with the total irreversible cyclic plastic microdeformations in a cycle (the most representative of fatigue damage [1]) in conjunction with the concept of FFE to estimate fatigue life.

Eq. (6) can be used to predict this material's fatigue life within the

assessed fatigue life scales for arbitrary load amplitudes. N_f is the fatigue life to failure, T_{ss} is the steady-state temperature in Stage II of Fig. 5, and \dot{w}_p is the plastic strain energy per cycle as obtained by the SEPSE method. To illustrate the application of FFE, consider, for example, a component being tested at an environmental temperature of 204 °C. It is desired to predict its useful life at 100 MPa. Based on the SEPSE algorithm, the PSE per cycle at this load is $6.154 \times 10^4 \frac{J}{m^3 \text{ cycle}}$. The predicted steady-state temperature via the FEM code is 477.8 K. Using the FFE relation in Eq. (5) with the average FFE value of $14.6 \frac{MJ}{m^3 \text{ K}}$, the fatigue life for this load amplitude is estimated to be 113,146 cycles. Considering that the experimentally obtained fatigue life for this loading condition is 125,600 cycles, the error of fatigue life estimation, in this case, is 9.9 %. Therefore, it can be concluded that the microstructure-sensitive algorithm reliably predicts the fatigue life.

6. Conclusions

Additively manufactured C-18150 copper alloy, via LB-PBF, is cyclically loaded at room and elevated environmental temperatures. Two methods are used to measure the amount of cyclic damage at different stress amplitude and temperatures. In one method, the area inside the stress–strain hysteresis curve is used to calculate the plastic strain energy as the representative of fatigue damage. In another approach, a recently developed microstructure-sensitive and algorithm based on the statistical distribution of cyclic microplastic strains—implemented from the stress–strain data of a monotonic tensile test—is used. The results show that the irreversible damage at room and elevated temperatures obtained via the two methods agree. Hence, the SEPSE can be used for the analysis of AM specimens at room and elevated temperatures.

Using the finite element method to calculate the specimen's surface temperature for different load cases, fracture fatigue Entropy (FFE) is determined. It was shown that FFE stays within a narrow range and is constant for the experimented temperature range. Therefore, the microstructure-sensitive algorithm may be used to estimate fatigue life and analyze additively manufactured specimens at elevated temperatures. This type of analysis can have great implications in the fatigue study of additively manufactured materials at room and elevated temperatures where newly-developed materials with desired fatigue behavior/properties need to be rapidly assessed to understand the relative effect of adding/removing one chemical ingredient from their composition.

Declaration of Competing Interest

The authors declare that they have no known competing financial interests or personal relationships that could have appeared to influence the work reported in this paper.

Acknowledgments

This paper describes objective technical results and analysis. Any subjective views or opinions that might be expressed in the paper do not necessarily represent the views of the National Aeronautics and Space Administration (NASA) or the United States Government. This work is supported by the National Aeronautics and Space Administration (NASA)'s Established Program to Stimulate Competitive Research (EPSCoR) Cooperative Agreement numbers 80NSSC19M0079 and 80NSSC20M0149 (CFDA number 43.008). The use of instruments housed within the LSU Shared Instrumentation Facilities (SIF), a part of LAMDA (grant number NSF #OIA-1946231) Core User Facilities, is acknowledged. The L-PBF samples are prepared by Moog (www.moog.com).

References

- [1] Jirandehi AP, Khonsari MM. General quantification of fatigue damage with provision for microstructure: a review. Fatigue Fract Eng Mater Struct 2021;44(8):
- [2] Gorelik M. Additive manufacturing in the context of structural integrity. Int J Fatigue 2017;94:168–77.
- [3] Sanaei N, Fatemi A. Defects in additive manufactured metals and their effect on fatigue performance: a state-of-the-art review. Prog Mater Sci 2021;117:100724. https://doi.org/10.1016/j.pmatsci.2020.100724.
- [4] McDowell DL, Gall K, Horstemeyer MF, Fan J. Microstructure-based fatigue modeling of cast A356–T6 alloy. Eng Fract Mech 2003;70(1):49–80.
- [5] Murakami Y, Endo M. Effects of defects, inclusions and inhomogeneities on fatigue strength. Int J Fatigue 1994;16(3):163–82.
- [6] Wegener T, Koopmann J, Richter J, Krooß P, Niendorf T. CuCrZr processed by laser powder bed fusion—processability and influence of heat treatment on electrical conductivity, microstructure and mechanical properties. Fatigue Fract Eng Mater Struct 2021;44(9):2570–90.
- [7] Sangid MD. The physics of fatigue crack initiation. Int J Fatigue 2013;57:58-72.
- [8] Le V-D, Pessard E, Morel F, Prigent S. Fatigue behaviour of additively manufactured Ti-6Al-4V alloy: the role of defects on scatter and statistical size effect. Int J Fatigue 2020;140:105811.
- [9] Hajshirmohammadi B, Khonsari M. An approach for fatigue life prediction based on external heating. Int J Mech Sci 2021;204:106510.
- [10] Hajshirmohammadi B, Khonsari M. On the entropy of fatigue crack propagation. Int J Fatigue 2020:133:105413.
- [11] Ghadimi H, Jirandehi AP, Nemati S, Guo S. Small-sized specimen design with the provision for high-frequency bending-fatigue testing. Fatigue Fract Eng Mater Struct 2021;44(12):3517–37.
- [12] Pegues JW, Shamsaei N, Roach MD, Williamson RS. Fatigue life estimation of additive manufactured parts in the as-built surface condition. Mater Des Process Commun 2019;1(3). https://doi.org/10.1002/mdp2.v1.310.1002/mdp2.36.
- [13] Lee S, Rasoolian B, Silva DF, Pegues JW, Shamsaei N. Surface roughness parameter and modeling for fatigue behavior of additive manufactured parts: a nondestructive data-driven approach. Addit Manuf 2021;46:102094. https://doi.org/ 10.1016/j.addma.2021.102094.
- [14] Lee S, Pegues JW, Shamsaei N. Fatigue behavior and modeling for additive manufactured 304L stainless steel: the effect of surface roughness. Int J Fatigue 2020;141:105856. https://doi.org/10.1016/j.ijfatigue.2020.105856.
- [15] Meneghetti G, Rigon D, Gennari C. An analysis of defects influence on axial fatigue strength of maraging steel specimens produced by additive manufacturing. Int J Fatigue 2019:118:54–64.
- [16] Hu Y, Wu S, Wu Z, Zhong X, Ahmed S, Karabal S, et al. A new approach to correlate the defect population with the fatigue life of selective laser melted Ti-6Al-4V alloy. Int J Fatigue 2020;136:105584.
- [17] Hung C-H, Chen W-T, Sehhat MH, Leu MC. The effect of laser welding modes on mechanical properties and microstructure of 304L stainless steel parts fabricated by laser-foil-printing additive manufacturing. Int. J. Adv. Manuf. Technol. 2021; 112(3-4):867-77.
- [18] Zhan Z, Li H. Machine learning based fatigue life prediction with effects of additive manufacturing process parameters for printed SS 316L. Int J Fatigue 2021;142: 105941.
- [19] Prithivirajan V, Sangid MD. Examining metrics for fatigue life predictions of additively manufactured IN718 via crystal plasticity modeling including the role of simulation volume and microstructural constraints. Mater Sci Eng, A 2020;783: 139312
- [20] Molaei R, Fatemi A, Sanaei N, Pegues J, Shamsaei N, Shao S, et al. Fatigue of additive manufactured Ti-6Al-4V, Part II: The relationship between microstructure, material cyclic properties, and component performance. Int J Fatigue 2020;132: 105363.
- [21] Ziółkowski G, Chlebus E, Szymczyk P, Kurzac J. Application of X-ray CT method for discontinuity and porosity detection in 316L stainless steel parts produced with SLM technology. Arch Civil Mech Eng 2014;14(4):608–14.
- [22] Chen Bo, Jiang J, Dunne FPE. Is stored energy density the primary meso-scale mechanistic driver for fatigue crack nucleation? Int J Plast 2018;101:213–29.
- [23] Ou C-Y, Voothaluru R, Liu CR. Fatigue crack initiation of metals fabricated by additive manufacturing—a crystal plasticity energy-based approach to IN718 life prediction. Crystals 2020;10(10):905.
- [24] Wilson D, Wan W, Dunne FPE. Microstructurally-sensitive fatigue crack growth in HCP, BCC and FCC polycrystals. J Mech Phys Solids 2019;126:204–25.
- [25] Bandyopadhyay R, Prithivirajan V, Peralta AD, Sangid MD. Microstructuresensitive critical plastic strain energy density criterion for fatigue life prediction across various loading regimes. Proc Royal Soc A 2020;476(2236):20190766. https://doi.org/10.1098/rspa.2019.0766.
- [26] Douellou C, Balandraud X, Duc E, Verquin B, Lefebvre F, Sar F. Fast fatigue characterization by infrared thermography for additive manufacturing. Procedia Struct Integrity 2019;19:90–100.
- [27] Blakey-Milner B, Gradl P, Snedden G, Brooks M, Pitot J, Lopez E, et al. Metal additive manufacturing in aerospace: a review. Mater Des 2021;209:110008. https://doi.org/10.1016/j.matdes.2021.110008.
- [28] Zhang X, Wang T, Gong X, Li Q, Liu Y, Wang Q, et al. Low cycle fatigue properties, damage mechanism, life prediction and microstructure of MarBN steel: influence of temperature. Int J Fatigue 2021;144:106070. https://doi.org/10.1016/j. ijfatigue.2020.106070.
- [29] Popovich V, Borisov E, Heurtebise V, Riemslag T, Popovich A, Sufiiarov VS. Creep and thermomechanical fatigue of functionally graded Inconel 718 produced by

- additive manufacturing. In: TMS annual meeting & exhibition, Springer; 2018. p. 85-97
- [30] Salvan C, Briottet L, Baffie T, Guetaz L, Flament C. CuCrZr alloy produced by laser powder bed fusion: microstructure, nanoscale strengthening mechanisms, electrical and mechanical properties. Mater Sci Eng, A 2021;826:141915. https://doi.org/10.1016/j.msea.2021.141915.
- [31] Wallis C, Buchmayr B. Effect of heat treatments on microstructure and properties of CuCrZr produced by laser-powder bed fusion. Mater Sci Eng, A 2019;744:215–23.
- [32] Buchmayr B, Panzl G, Walzl A, Wallis C. Laser powder bed fusion-materials issues and optimized processing parameters for tool steels, AlSiMg-and CuCrZr-alloys. Adv Eng Mater 2017;19(4):1600667.
- [33] Gradl PR, Protz C, Greene SE, Ellis D, Lerch B, Locci I. Development and hot-fire testing of additively manufactured copper combustion chambers for liquid rocket engine applications. In: 53rd AIAA/SAE/ASEE joint propulsion conference; 2017. p. 4670.
- [34] Kerstens F, Cervone A, Gradl P. End to end process evaluation for additively manufactured liquid rocket engine thrust chambers. Acta Astronaut 2021;182: 454–65
- [35] Gradl PR, Protz CS, Cooper K, Ellis D, Evans LJ, Garcia C. GRCop-42 Development and Hot-fire testing using additive manufacturing powder bed fusion for channelcooled combustion chambers. In: AIAA propulsion and energy 2019 forum; 2019. p. 4228.
- [36] Gradl PR, Protz CS, Zagorski K, Doshi V, McCallum H. Additive manufacturing and hot-fire testing of bimetallic GRCop-84 and C-18150 channel-cooled combustion chambers using powder bed fusion and inconel 625 hybrid directed energy deposition. In: AIAA propulsion and energy 2019 forum; 2019. p. 4390.
- [37] Demeneghi G, Barnes B, Gradl P, Mayeur JR, Hazeli K. Size effects on microstructure and mechanical properties of additively manufactured copper-chromium-niobium alloy. Mater Sci Eng, A 2021;820:141511.
- [38] Minneci RP, Lass EA, Bunn JR, Choo H, Rawn CJ. Copper-based alloys for structural high-heat-flux applications: a review of development, properties, and performance of Cu-rich Cu-Cr-Nb alloys. Int Mater Rev 2021;66(6):394-425.
- [39] Jahns K, Bappert R, Böhlke P, Krupp U. Additive manufacturing of CuCr1Zr by development of a gas atomization and laser powder bed fusion routine. Int J Adv Manuf Technol 2020;107(5-6):2151–61.
- [40] Morrow J. Cyclic plastic strain energy and fatigue of metals, Internal friction, damping, and cyclic plasticity. ASTM International; 1965.
- [41] Garud Y. A new approach to the evaluation of fatigue under multiaxial loadings, 1981.
- [42] Klemenc J, Šeruga D, Nagode A, Nagode M. Comprehensive modelling of the hysteresis loops and strain-energy density for low-cycle fatigue-life predictions of the AZ31 magnesium alloy. Materials 2019;12(22):3692.
- [43] Houwink R. Elasticity, plasticity, and structure of matter; 1954.
- [44] Cai W, Bulatov VV, Chang J, Li J, Yip S. Dislocation core effects on mobility. Dislocat Solids 2004;12(1).
- [45] Fantozzi G, Ritchie I. Internal friction caused by the intrinsic properties of dislocations. Le J de Physique Colloques 1981;42(C5):C5-3-5-23.
- [46] Mason WP, Wehr J. Internal friction and ultrasonic yield stress of the alloy 90 Ti 6 Al 4 V. J Phys Chem Solids 1970;31(8):1925–33.
- [47] Guo Q, Guo X. Research on high-cycle fatigue behavior of FV520B stainless steel based on intrinsic dissipation. Mater Des 2016;90:248–55.
- [48] Zener C. Internal friction in solids. I. Theory of internal friction in reeds. Phys Rev 1937;52(3):230–5.
- [49] Charkaluk E, Constantinescu A. Dissipative aspects in high cycle fatigue. Mech Mater 2009;41(5):483–94.
 [50] Meneghetti G, Quaresimin M. Fatigue strength assessment of a short fiber
- 50) Menegnetti G, Quaresimin M. Fatigue strength assessment of a snort noer composite based on the specific heat dissipation. Compos B Eng 2011;42(2): 217–25.
- [51] Liakat M, Khonsari MM. On the anelasticity and fatigue fracture entropy in highcycle metal fatigue. Mater Des 2015;82:18–27.
- [52] Haghshenas A, Jang J, Khonsari M. On the intrinsic dissipation and fracture fatigue entropy of metals. Mech Mater 2021;155:103734.
- [53] Wertz J, Shen M-H-H, Scott-Emuakpor O, George T, Cross C. An energy-based torsional-shear fatigue lifing method. Exp Mech 2012;52(7):705–15.
- [54] Ozaltun H. An energy based fatigue lifing method for in-service components and numerical assessment of U10Mo alloy based fuel mini plates. The Ohio State University; 2011.
- [55] McGuire SM, Fine ME, Buck O, Achenbach JD. Nondestructive detection of fatigue cracks in PM 304 stainless steel by internal friction and elasticity. J Mater Res 1993:8(9):2216–23.
- [56] Blanter MS, Golovin IS, Neuhauser H, Sinning H. Internal friction in metallic materials. A Handbook 2007;540:1–144.
- [57] Roebben G, Donzel L, Steen M, Schaller R, Van der Biest O. Fatigue resistant silicon nitride ceramics due to anelastic deformation and energy dissipation. J Alloy Compd 2000;310(1-2):39–43.
- [58] Jirandehi AP, Khonsari M. On the determination of cyclic plastic strain energy with the provision for microplasticity. Int J Fatigue 2020;142:105966.
- [59] Musienko A, Tatschl A, Schmidegg K, Kolednik O, Pippan R, Cailletaud G. Threedimensional finite element simulation of a polycrystalline copper specimen. Acta Mater 2007;55(12):4121–36.
- [60] Chen J, Salvati E, Uzun F, Papadaki C, Wang Z, Everaerts J, et al. An experimental and numerical analysis of residual stresses in a TIG weldment of a single crystal nickel-base superalloy. J Manuf Processes 2020;53:190–200.
- [61] Chen B. Understanding microstructurally-sensitive fatigue crack nucleation in superalloys. Department of Materials Imperial College London; 2018.

- [62] Chen J, Korsunsky AM. Why is local stress statistics normal, and strain lognormal? Mater Des 2021;198:109319.
- [63] Milne I, Ritchie RO, Karihaloo BL. Comprehensive structural integrity: cyclic loading and fatigue. Elsevier; 2003.
- [64] Bishop JFW, Hill R. CXXVIII. A theoretical derivation of the plastic properties of a polycrystalline face-centred metal. The Lond Edinburgh Dublin Philos Magazine J Sci 1951;42(334):1298–307.
- [65] Esin A, Jones WJD. A statistical approach to micro-plastic strain in metals. J Strain Anal 1966;1(5):415–21.
- [66] Khonsari MM, Amiri M. Introduction to thermodynamics of mechanical fatigue. CRC press; 2012.
- [67] Jirandehi AP, Khonsari M. Microstructure-sensitive estimation of fatigue life using cyclic thermodynamic entropy as an index for metals. Theor Appl Fract Mech 2021; 112:102854.
- [68] Naderi M, Amiri M, Khonsari M. On the thermodynamic entropy of fatigue fracture. Proc Royal Soc A: Math Phys Eng Sci 2010;466(2114):423–38.
- [69] Mehdizadeh M, Khonsari M. On the application of fracture fatigue entropy to multiaxial loading. Int J Fatigue 2021;150:106321.
- [70] Ribeiro P, Petit J, Gallimard L. Experimental determination of entropy and exergy in low cycle fatigue. Int J Fatigue 2020;136:105333.

- [71] Huang J, Li C, Liu W. Investigation of internal friction and fracture fatigue entropy of CFRP laminates with various stacking sequences subjected to fatigue loading. Thin-Walled Struct 2020;155:106978.
- [72] Zeng C, Wen H, Bernard BC, Raush JR, Gradl PR, Khonsari M, et al. Effect of temperature history on thermal properties of additively manufactured C-18150 alloy samples. Manufact Lett 2021;28:25–9.
- [73] Letcher T, Shen M-H- H, Scott-emuakpor O, George T, Cross C. An energy-based critical fatigue life prediction method for AL6061-T6. Fatigue Fract Eng Mater Struct 2012;35(9):861–70.
- [74] Scott-Emuakpor OE, George TJ, Cross CJ, Shen M-H- H. Analysis of strain energy behavior throughout a fatigue process. Exp Mech 2011;51(8):1317–23.
- [75] Liakat M, Khonsari MM. Rapid estimation of fatigue entropy and toughness in metals. Mater Des 2014;62:149–57.
- [76] Bai Y, Zhao C, Zhang Yu, Chen J, Wang H. Additively manufactured CuCrZr alloy: microstructure, mechanical properties and machinability. Mater Sci Eng, A 2021; 819:141528. https://doi.org/10.1016/j.msea.2021.141528.
- [77] Jirandehi AP, Mehdizadeh M, Khonsari M. Temperature-induced buckling of ductile metals during cyclic loading and the subsequent early fracture. Int J Mech Sci 2020;176:105525.